Volume 13
Number 15
21 April 2021
Pages 6999-7414

Nanoscale

rsc.li/nanoscale

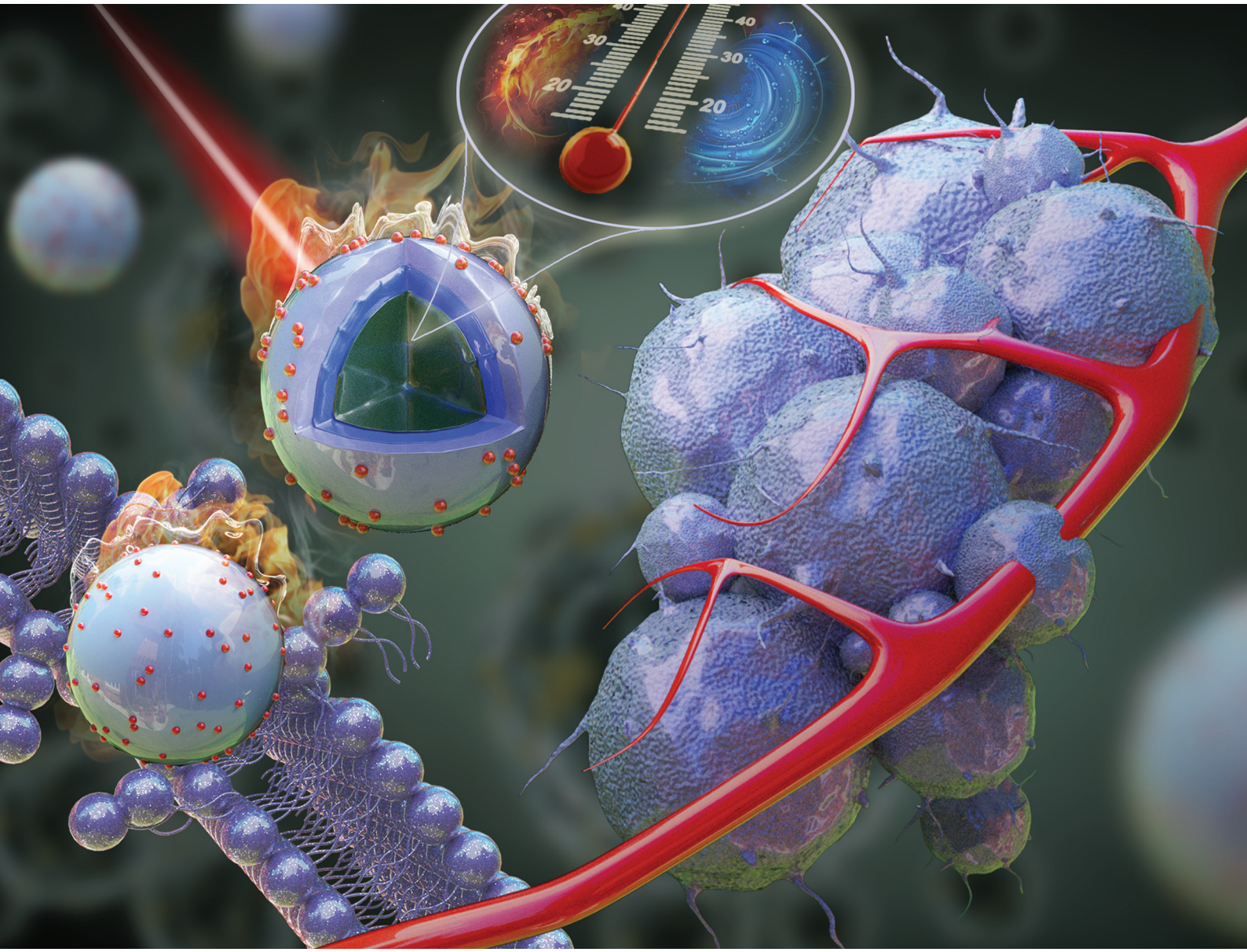

ISSN 2040-3372

ROYAL SOCIETY OF CHEMISTRY

PAPER

Guotao Xiang, Xiaojun Wang, Jiahua Zhang *et al.*
Upconversion nanoparticles modified by Cu_2S for photothermal therapy along with real-time optical thermometry

NCNST

Nanoscale

PAPER

View Article Online
View Journal | View Issue

Cite this: *Nanoscale*, 2021, **13**, 7161

Upconversion nanoparticles modified by Cu_2S for photothermal therapy along with real-time optical thermometry†

Guotao Xiang, *[a] Qing Xia,[a] Xiaotong Liu,[a] Yongjie Wang,[a] Sha Jiang,[a] Li Li,[a] Xianju Zhou,[a] Li Ma,[b] Xiaojun Wang*[b] and Jiahua Zhang *[c]

Highly effective photothermal conversion performance coupled with high resolution temperature detection in real time is urgently needed for photothermal therapy (PTT). Herein, ultra-small Cu_2S nanoparticles (NPs) were designed to absorb on the surface of $NaScF_4$: $Yb^{3+}/Er^{3+}/Mn^{2+}$@$NaScF_4$@SiO_2 NPs to form a central-satellite system, in which the Cu_2S NPs play the role of providing significant light-to-heat conversion ability and the Er^{3+} ions in the $NaScF_4$: $Yb^{3+}/Er^{3+}/Mn^{2+}$ cores act as a thermometric probe based on the fluorescence intensity ratio (FIR) technology operating in the biological windows. A wavelength of 915 nm is used instead of the conventional 980 nm excitation wavelength to eliminate the laser induced overheating effect for the bio-tissues, by which Yb^{3+} can also be effectively excited. The temperature resolution of the FIR-based optical thermometer is determined to be better than 0.08 K over the biophysical temperature range with a minimal value of 0.06 K at 298 K, perfectly satisfying the requirements of biomedicine. Under the radiation of 915 nm light, the Cu_2S NPs exhibit remarkable light-to-heat conversion capacity, which is proved by photothermal ablation testing of *E. coli*. The results reveal the enormous potential of the present NPs for PTT integrated with real-time temperature sensing with high resolution.

Received 26th December 2020,
Accepted 22nd March 2021

DOI: 10.1039/d0nr09115d

rsc.li/nanoscale

Introduction

Photothermal therapy (PTT) is a newly developed cancer treatment technology with the advantages of high selectivity, minimal invasiveness and fewer side-effects.[1–5] Therein, nanosized PTT agents, which are of vital importance during the PTT process, can destroy tumors irreversibly through releasing heat converted from near infrared (NIR) light. To date, a large number of nanomaterials are employed as PTT agents, such as metal nanoparticles (NPs), metal sulfides, carbon NPs and so on.[6–16] Among the various types of PTT agents, copper-based NPs are confirmed to be promising candidates for PTT due to their facile synthesis, low toxicity and good stability as well as their remarkable photothermal conversion efficiency.[17–21]

Meanwhile, precise temperature control in real time is also vitally important for PTT to avoid injury to normal cells caused by the overheating effect. Moreover, cancer cells are very sensitive to the temperature. For instance, HeLa cells present a survival rate of about 11% at 43 °C but their viability is increased by five times with a temperature decrease of 0.2 °C.[22] That is to say, the temperature determination for PTT should possess the feature of excellent resolution to guarantee the optimal temperature for destroying the tumor cells. Nanosized upconversion (UC) optical thermometers based on fluorescence intensity ratio (FIR) technology are a promising way to afford the requirements mentioned above because of their superior properties in biological applications such as negligible auto-fluorescence, low toxicity, strong anti-jamming capacity, high spatial resolution, *etc.*[23–36]

In particular, 980 nm-driven Yb^{3+}/Er^{3+} co-doped UCNPs are frequently reported as prospective optical thermometers based on FIR between the thermally coupled levels (TCLs) of Er^{3+}: $^2H_{11/2}/^4S_{3/2}$.[37–43] However, their practical applications are severely restricted by the shallow penetration depth in biological specimens and the 980 nm laser induced overheating effect, resulting from the strong optical absorption of water and biological tissues for light located in the ranges of 500 nm–600 nm and 930 nm–1030 nm.[44] This technical barrier can be removed by reselecting the driven and operating wavelength of the Yb^{3+}/Er^{3+} co-doped UC thermal sensors.

[a]*Department of Mathematics and Physics, Chongqing University of Posts and Telecommunications, 2 Chongwen Road, Chongqing 400065, China. E-mail: xianggt@cqupt.edu.cn*
[b]*Department of Physics & Astronomy, Georgia Southern University, Statesboro, Georgia 30460, USA. E-mail: xwang@georgiasouthern.edu*
[c]*State Key Laboratory of Luminescence and Applications, Changchun Institute of Optics, Fine Mechanics and Physics, Chinese Academy of Sciences, 3888 Eastern South Lake Road, Changchun 130033, China. E-mail: zhangjh@ciomp.ac.cn*
†Electronic supplementary information (ESI) available. See DOI: 10.1039/d0nr09115d

Actually, the Yb^{3+} ion can be effectively pumped to its excited state by 915 nm wavelength followed by efficient energy transfer (ET) processes to the Er^{3+} ion, which was previously demonstrated by Zhan *et al.*[45] More importantly, since the absorption coefficient of biological tissues at 915 nm is much lower than that at 980 nm, the laser induced overheating effect can be eliminated along with the improvement of detection depth of the UCNPs in biological specimens through the replacement of excitation wavelength.[46] Beyond that, the thermally coupled Stark sublevels of Er^{3+}: $^4F_{9/2}$ manifold locating just in the biological window can be selected for FIR-based optical thermometry instead of the green emitting levels Er^{3+}: $^2H_{11/2}/^4S_{3/2}$, by which a high sensitive temperature sensing performance can be realized, especially in the physiological temperature region.[47–49]

Hexagonal phase $NaScF_4$: $Yb^{3+}/Er^{3+}/Mn^{2+}$ has been established to be extremely efficient UCNPs with approximately monochromatic red emission derived from the Er^{3+}: $^4F_{9/2} \rightarrow {}^4I_{15/2}$ transition.[50] In this paper, $NaScF_4$: $Yb^{3+}/Er^{3+}/Mn^{2+}$ is further built to be a central-satellite structure, expressed as $NaScF_4$: $Yb^{3+}/Er^{3+}/Mn^{2+}$@$NaScF_4$@SiO_2@Cu_2S. Under excitation of 915 nm wavelength, the as-prepared NPs present excellent temperature sensing behavior based on the FIR between the thermally coupled Stark sublevels of Er^{3+}: $^4F_{9/2}$ manifold along with an outstanding light-to-heat conversion performance realized by the ultra-small Cu_2S NPs, which is certified by the photothermal ablation testing of *E. coli*. The temperature resolution of the FIR-based optical thermometer is superior to 0.08 K within the biophysical temperature range, wonderfully meeting the requirements of biological applications.[51] All the findings indicate that $NaScF_4$: $Yb^{3+}/Er^{3+}/Mn^{2+}$@$NaScF_4$@SiO_2@Cu_2S can afford effective photothermal conversion with high resolution optical thermometry in real time.

Experimental

Chemicals

Rare earth chloride $ScCl_3$ (99.999%), $YbCl_3$ (99.999%) and $ErCl_3$ (99.999%) are supplied by Beijing Founde Star Science & Technology Co, Ltd. Oleic acid (OA, 90%) and 1-octadecene (ODE, 90%) are obtained from Alfa Aesar. CO-520, tetraethoxysilane (TEOS) and aminopropyltrimethoxysilane (APTMS) are purchased from Aladdin. $MnCl_2$, NH_4F, NaOH, NH_4OH (30 wt%), $Na_2S{\cdot}9H_2O$, $CuCl_2{\cdot}2H_2O$, $Na_3C_6H_5O_7{\cdot}2H_2O$, cyclohexane, acetone, ethanol and methanol are supplied by Chongqing Chuandong Chemical (Group) Co, Ltd. Phosphate buffered saline (PBS), nutrient broth and agar medium are acquired from Beijing Land Bridge Technology Co, Ltd. *Escherichia coli* (ATCC25922) is purchased from Shanghai Luwei Technology Co, Ltd. All the reagents are used for the present experiments directly without further purification.

Synthesis of $NaScF_4$: 20% Yb^{3+}/2% Er^{3+}/10% Mn^{2+} and $NaScF_4$: 20% Yb^{3+}/2% Er^{3+}/10% Mn^{2+}@$NaScF_4$

The preparation process of $NaScF_4$: 20% Yb^{3+}/2% Er^{3+}/10% Mn^{2+} (NYEM) UCNPs is according to our previous paper.[50] The obtained NYEM are dispersed in 4 mL cyclohexane for the synthesis of NYEM@$NaScF_4$. Specifically, 12 mL OA and 28 mL ODE along with 0.8 mmol $ScCl_3$ are mixed in a 100 mL three-neck round-bottom flask and then reacted at 140 °C for 0.5 h. After that, the solution temperature is cooled down to 80 °C and 4 mL cyclohexane containing 0.8 mmol NYEM is injected into the flask. The reaction solution is kept at 80 °C for 0.5 h to clear away the cyclohexane. Whereafter, 0.8 mmol NaOH and 3.2 mmol NH_4F dissolved in 10 mL methanol are injected into the flask and the solution temperature is maintained at 80 °C for another 0.5 h to remove the residual methanol. Next, the reaction solution is heated to 300 °C and kept for 1.5 h. Finally, the temperature of the solution is naturally decreased to room temperature. The products are obtained through the addition of excess ethanol and centrifugation as well as washing with ethanol three times. The reaction solution is stirred by a magnetic mixer and protected by nitrogen environment during the whole preparation process.

Synthesis of NYEM@$NaScF_4$@SiO_2

The obtained NYEM@$NaScF_4$ is mixed with 10 mL cyclohexane and 0.1mL CO-520 in a 25 mL beaker and stirred for 10 min. Next, 0.4 mL CO-520 and 0.08 mL NH_4OH are added into the solution and sonicated under sealed conditions for 20 min to form a transparent emulsion. Subsequently, the solution continues to be rotated for 12 h after the addition of 0.04 mL TEOS. Finally, the NYEM@$NaScF_4$@SiO_2 is precipitated by injecting acetone and washed with water and ethanol several times.

Synthesis of NYEM@$NaScF_4$@SiO_2@Cu_2S

A typical method reported by a previous paper is used for the synthesis of ultra-small Cu_2S NPs.[52] Firstly, 2 mL $Na_2S{\cdot}9H_2O$ (0.04 M) is added into 100 mL aqueous solutions containing 0.014 g $CuCl_2{\cdot}2H_2O$ and 0.02 g $Na_3C_6H_5O_7{\cdot}2H_2O$. Then, the solution is heated to 90 °C and maintained for 20 min under stirring condition to form the Cu_2S NPs solution with a dark green color, which is stored in ice water at 4 °C for further use. Meanwhile, 0.15 mL APTMS is injected dropwise into a 50 mL ethanol solution containing 0.1 g NYEM@$NaScF_4$@SiO_2 along with stirring for 12 h. Then, 40 mL Cu_2S NPs solution is mixed with the modified NYEM@$NaScF_4$@SiO_2 and stirred for 2 h. Finally, the products are obtained by centrifugation and washed with water and ethanol several times.

Photothermal ablation of bacteria

E. coli is firstly introduced into the sterile nutrient broth and diluted with sterile water. Next, the same amount of bacterial solutions are separated into four flasks, named Group control, Group NIR, Group UCNPs and Group UCNPs + NIR, respectively. Then, 100 μL PBS buffer solutions are added into the flasks of the Group control and Group NIR, respectively. Meanwhile, both Group UCNPs and Group UCNPs + NIR are mixed with 100 μL PBS solutions containing NYEM@$NaScF_4$@SiO_2@Cu_2S (1 mg mL^{-1}). After that, the four groups of bacterial solutions are moved to the corresponding

agar mediums. Moreover, 915 nm light with a power density of 12 mW mm^{-2} is employed to irradiate Group NIR and Group UCNPs + NIR for 15 min. Finally, all the agar media are placed in a constant temperature incubator at 37 °C for 24 h in air and then taken out to observe the colony amount of every group.

Characterization

A Persee XD-2 diffractometer is utilized to acquire the powder X-ray diffraction (XRD) data. The morphology and element analysis of the samples dispersed on the carbon-coated nickel grid are measured by a JEOL JEM 2100 transmission electron microscope equipped with an energy-dispersive X-ray spectrometer. A Cary 5000 UV–vis–NIR spectrophotometer is employed to measure the absorption spectra. The spectra data are collected by a FLS1000 spectrometer with a 915 nm laser as the excitation source as well as a home-made electric furnace to control the temperature of the prepared samples. A thermocouple thermometer supplied by Digi-Sense with a resolution of 0.1 K is used to monitor the photothermal conversion effect.

Results and discussion

Structure and morphology

As illustrated in Fig. 1(a), a reasonable and comprehensive process is designed for the preparation of NYEM@$NaScF_4$@SiO_2@Cu_2S, including four subprocesses. Firstly, a solvothermal process is utilized to synthesize the NYEM UCNPs as the core structure. Secondly, a similar approach is employed to epitaxially grow a $NaScF_4$ shell for the purpose of UC enhancement. After that, a thin silica shell is coated on the surface of NYEM@$NaScF_4$ to make the sample hydrophilic. Finally, ultrasmall Cu_2S NPs with a negative charge are attached on the APTMS-modified NYEM@$NaScF_4$@SiO_2 by electrostatic adsorption.[53] The XRD patterns of the samples synthesized at various steps are exhibited in Fig. 1(b) to determine their phase purity. Obviously, the positions and relative intensities of diffraction peaks of all the as-prepared samples are in good accordance with the hexagonal phase $NaScF_4$ with the space group $P3_1$. The characteristic peaks of neither SiO_2 nor Cu_2S are observed after the corresponding coating processes caused by a tiny amount of them existing in the samples.

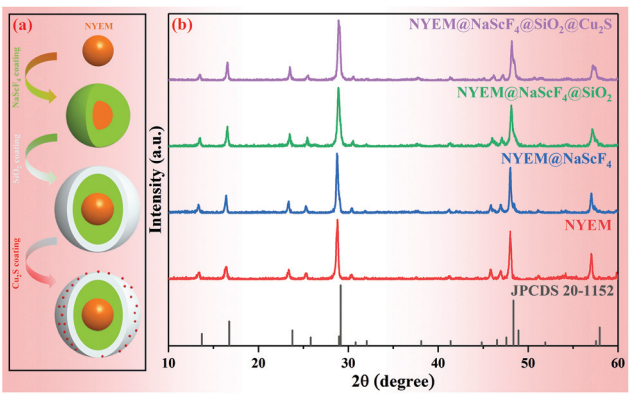

Fig. 1 (a) A description of the preparation of NYEM@$NaScF_4$@SiO_2@Cu_2S. (b) XRD diffraction patterns of the samples synthesized at various steps along with the reference data of hexagonal $NaScF_4$ (JCPDS 20-1152).

The morphology and size evolution of the present samples are detected by TEM images, as shown in Fig. 2(a)–(d). The NYEM displays a monodisperse sphere with a mean diameter of 40 nm (Fig. 2(a)). After the epitaxial growth of the $NaScF_4$ shell, the spherical UCNPs transform into a regular cube-like shape with an average size of approximately 44 nm (Fig. 2(b)). The energy-dispersive X-ray spectroscopy (EDS) line profiles of NYEM and NYEM@$NaScF_4$ are measured to verify the successful encapsulation of the $NaScF_4$ shell. As shown in Fig. S1,† the elements of Yb, Er and Mn are distributed uniformly in NYEM but they are mainly located in the interior of NYEM@$NaScF_4$, indicating the growth of the $NaScF_4$ shell without Yb^{3+}, Er^{3+} and Mn^{2+} doping. Subsequently, a layer of SiO_2 with 4 nm thickness is uniformly coated on the surface of NYEM@$NaScF_4$ to make the UCNPs hydrophilic (Fig. 2(c)). Finally, a certain amount of about 7 nm Cu_2S NPs is captured by the NYEM@$NaScF_4$@SiO_2 NPs because of the electrostatic interaction, constructing a so-called central-satellite system (Fig. 2(d)). As the high-resolution TEM (HR-TEM) image shows in Fig. 2(e), the interplanar spacing of the central core is measured to be 3.08 Å, corresponding to the (221) crystal plane of hexagonal phase $NaScF_4$ (JCPDS 20-1152). Furthermore, the lattice distance of the satellite particle is determined to be 2.04 Å, matching well with the (110) lattice plane of Cu_2S with the reference number JCPDS No. 26-1116. The element mapping images of a single NYEM@$NaScF_4$@SiO_2@Cu_2S particle are displayed in Fig. 2(f), clearly revealing the existence of all the elements, including Na, Sc, F, Yb, Er, Mn, Si, O, Cu and S. More importantly, it is distinctly observed that Na, Sc, F, Yb, Er and Mn are concentrated in the interior of the present particle. Oppositely, Si, O, Cu and S are distributed in the exterior of the same particle. The phenomenon mentioned above further demonstrates the successful construction of the NYEM@$NaScF_4$@SiO_2@Cu_2S central-satellite structure. The element of Er in NYEM@$NaScF_4$@SiO_2@Cu_2S displays quite a poor mapping signal, resulting from its extremely low doping concentration.

Luminescence properties

UC properties. The UC spectra of the samples prepared at various steps are detected by the excitation of the 915 nm wavelength. As depicted in Fig. 3(a), two weak green emission bands exist in the range of 500 nm–575 nm, attributed to the Er^{3+}: $^2H_{11/2}/^4S_{3/2} \rightarrow {}^4I_{15/2}$ transition. Besides that, a strong red emission appears in the region from 625 nm to 700 nm, belonging to Er^{3+}: $^4F_{9/2} \rightarrow {}^4I_{15/2}$ transition. Distinctly, compared with NYEM, the UC intensity of NYEM@$NaScF_4$ is sharply enhanced by the $NaScF_4$ shell, which is mainly ascribed to the suppression of ET processes from the Yb^{3+} ions to the particles' surface defects.[54] The significant enhancement of the Yb^{3+}: $^2F_{5/2} \rightarrow {}^2F_{7/2}$ transition shown in Fig. 3(b)

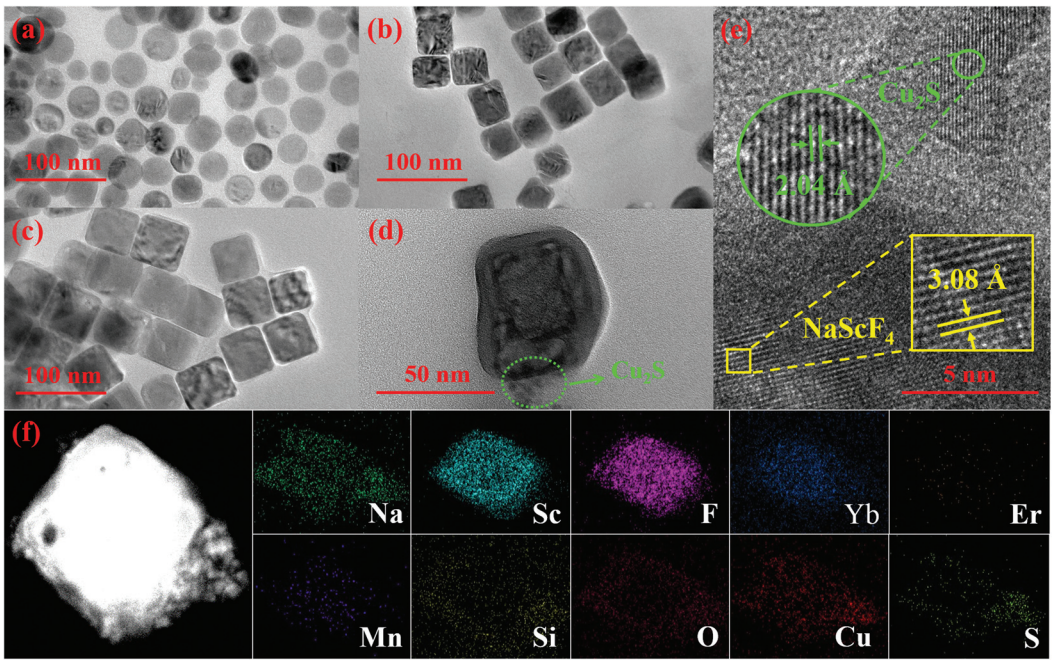

Fig. 2 TEM images of (a) NYEM, (b) NYEM@$NaScF_4$, (c) NYEM@$NaScF_4$@SiO_2 and (d) NYEM@$NaScF_4$@SiO_2@Cu_2S. (e) A HR-TEM image and (f) element mapping images of NYEM@$NaScF_4$@SiO_2@Cu_2S.

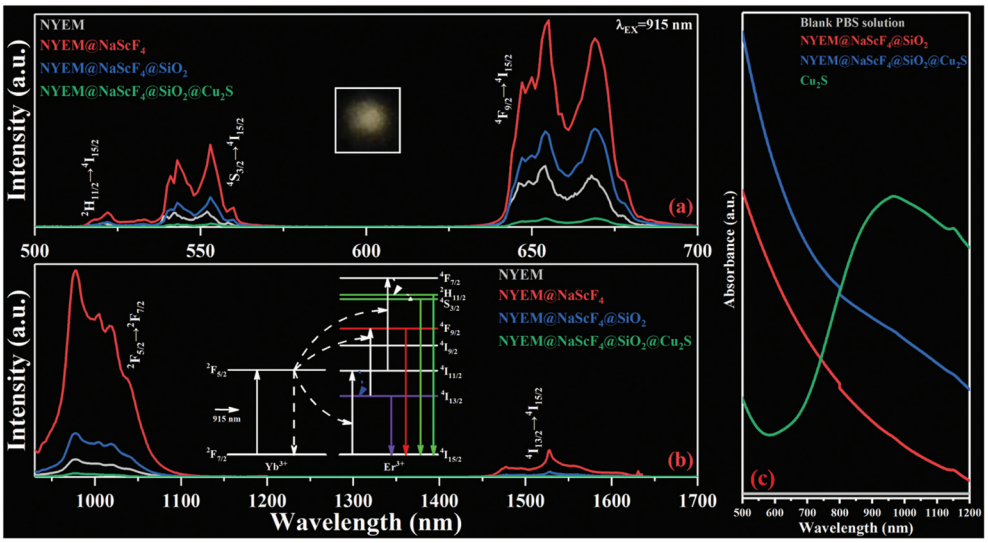

Fig. 3 (a) UC spectra and (b) NIR spectra of the prepared samples. (c) Absorption spectra of NYEM@$NaScF_4$@SiO_2, NYEM@$NaScF_4$@SiO_2@Cu_2S and Cu_2S dispersed in PBS solution as well as the blank PBS solution. The inset in (a) is the digital photo of NYEM@$NaScF_4$@SiO_2@Cu_2S excited by 915 nm wavelength. The inset in (b) is the ET processes between Yb^{3+} and Er^{3+}.

also provides compelling evidence for this. Meanwhile, after being shielded by the inert $NaScF_4$ shell, the intensity ratio (R/G) of the $^4F_{9/2} \rightarrow {}^4I_{15/2}$ transition (red) to $^2H_{11/2}/{}^4S_{3/2} \rightarrow {}^4I_{15/2}$ transition (green) is diminished obviously, which can be explained by the decrease of the non-radiative relaxation (NR) rate from the Er^{3+}: $^4I_{11/2}$ state to the $^4I_{13/2}$ state. As illustrated in the inset of Fig. 3(b), in the current system, the Er^{3+}: $^2H_{11/2}/{}^4S_{3/2}$ levels are predominantly populated by the ET from the excited Yb^{3+} ion to the Er^{3+}: $^4I_{11/2}$ level and the ET process from the Yb^{3+}: $^2F_{5/2}$ level to the Er^{3+}: $^4I_{13/2}$ level is one of the population routes for Er^{3+}: $^4F_{9/2}$ level. Since the population of the Er^{3+}: $^4I_{13/2}$ level is mainly realized by the NR process from the Er^{3+}: $^4I_{11/2}$ level, it can be concluded that the value of R/G is severely influenced by the NR rate between them. As seen from Fig. 3(b) and Fig. S2(a),† in spite of the enhancement of the absolute emission intensity of the Er^{3+}: $^4I_{13/2} \rightarrow {}^4I_{15/2}$ transition through the $NaScF_4$ shell structure, its relative intensity to the Yb^{3+}: $^2F_{5/2} \rightarrow {}^2F_{7/2}$ transition is weakened, which reveals

the diminution of the NR rate from the Er^{3+}: $^4I_{11/2}$ to $^4I_{13/2}$ level, giving rise to the decrease of the R/G value. Subsequently, the UC intensities of NYEM@$NaScF_4$@SiO_2 and NYEM@$NaScF_4$@SiO_2@Cu_2S successively decrease due to the strong scattering of the silica layer and the effective absorption of the Cu_2S NPs.[20] To demonstrate the absorption effect of the Cu_2S NPs, the absorption spectra of NYEM@$NaScF_4$@SiO_2, NYEM@$NaScF_4$@SiO_2@Cu_2S and Cu_2S dispersed in PBS solution as well as the blank PBS solution are measured and displayed in Fig. 3(c). Distinctly, NYEM@$NaScF_4$@SiO_2@Cu_2S shows a much stronger absorption for red and NIR light than NYEM@$NaScF_4$@SiO_2, resulting from the intense absorption of the Cu_2S NPs in the region of 600 nm – 1200 nm. Nevertheless, the UC luminescence of NYEM@$NaScF_4$@SiO_2@Cu_2S can still be observed by the naked eye, as presented in the inset of Fig. 3(a). In addition, as shown in Fig. S2(b),† the R/G value of the prepared sample is decreased after being decorated with Cu_2S NPs because of the absorption effect of Cu_2S for red light.

Optical thermometry behaviors and photothermal effects

The temperature dependent red UC spectra of NYEM@$NaScF_4$@SiO_2@Cu_2S are measured under the excitation of the 915 nm wavelength to explore its thermal sensing properties. As presented in Fig. 4(a), the relative intensity of the Stark transition peaking at 654 nm to the Stark transition peaking at 669 nm monotonously increased with the rising temperature, manifesting their potential for FIR-based optical thermometry. Considering the small energy separation ΔE between them, the two Stark sublevels can be regarded as TCLs, of which FIR abides by the Boltzmann distribution law:

$$\mathrm{FIR} = I_{654}/I_{669} = B\exp(-\Delta E/k_B T). \quad (1)$$

Here, I_{654} and I_{669} are defined as the emission intensities of the corresponding Stark transitions. B is a constant, independent of temperature. k_B and T represent the Boltzmann constant and absolute temperature, respectively. According to eqn (1), the fitting curve of FIR with increasing temperature is obtained and exhibited in Fig. 4(b), by which the ΔE is computed to be 341 cm^{-1}, similar to the value calculated from the spectral data. Then, in order to evaluate the performance of the present optical thermometer, it is necessary to obtain its absolute sensitivity S_A and relative sensitivity S_R, which are deemed as the important points for temperature sensing and expressed as follows:

$$S_A = |\mathrm{d}(\mathrm{FIR})/\mathrm{d}T|, \quad (2)$$

$$S_R = |\mathrm{d}(\mathrm{FIR})/(\mathrm{FIR})\mathrm{d}T|. \quad (3)$$

As shown in Fig. 4(c), the S_A reaches its maximal value of 0.54% K^{-1} at the initial temperature and then decreased with the increasing temperature in the studied range. The S_R is represented by $490/T^2$ with a maximal value of 0.55% K^{-1} at the starting temperature. Another major parameter for optical thermometers, named temperature resolution δT, is also achieved through eqn (4):

$$\delta T = (\delta\mathrm{FIR}/\mathrm{FIR}) \times (1/S_R), \quad (4)$$

where δFIR/FIR represents the relative uncertainty of FIR and depends mainly on the instruments used for testing. In our case, the value of δFIR/FIR is estimated to be 0.033%.[55] Therefore, the δT in this work is determined to be superior to the resolution of 0.08 K within the current temperature range and its minimal value is 0.06 K at the beginning temperature, as depicted in Fig. 4(d). The great sensitivity and excellent resolution of NYEM@$NaScF_4$@SiO_2@Cu_2S NPs indicate its enormous potential for temperature sensing.[46]

To assess the photothermal conversion ability of the as-prepared samples, a real-time temperature detection for NYEM@$NaScF_4$@SiO_2 and NYEM@$NaScF_4$@SiO_2@Cu_2S dispersed in PBS solution (1 mg mL^{-1}) is conducted through a thermocouple thermometer with a resolution of 0.1 K. As plotted in Fig. 5(a), under the continuous excitation of the 915 nm wavelength with a fixed power density of 12 mW mm^{-2}, the temperature of NYEM@$NaScF_4$@SiO_2@Cu_2S rapidly increased from room temperature in the first two minutes and then reached its equilibrium temperature 316 K (43 °C) about three minutes later, resulting in a temperature

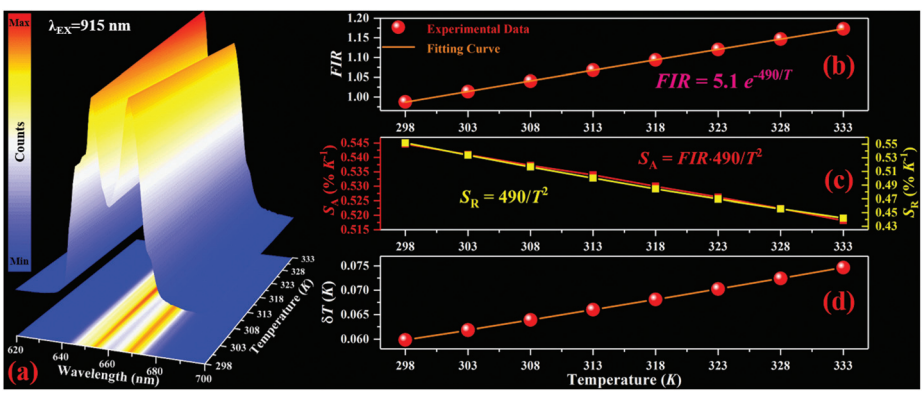

Fig. 4 (a) Red UC emission normalized at 669 nm, (b) FIR, (c) absolute sensitivity S_A and relative sensitivity S_R and (d) temperature resolution δT_G as a function of temperature in NYEM@$NaScF_4$@SiO_2@Cu_2S.

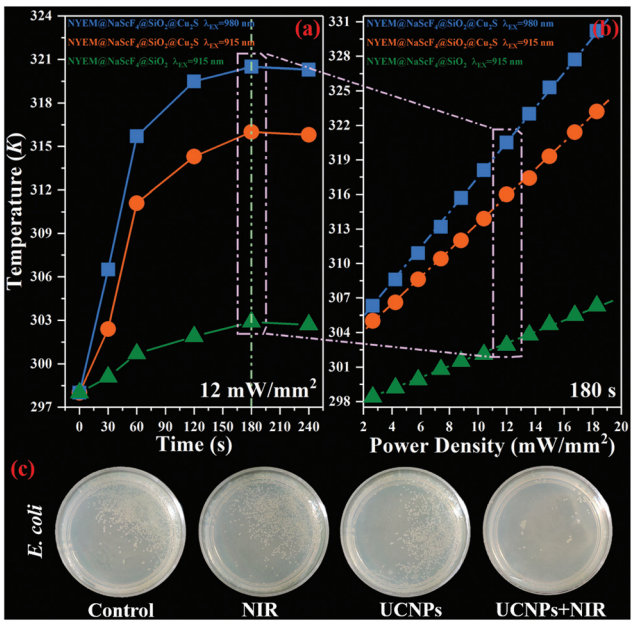

Fig. 5 The photothermal conversion effect of NYEM@$NaScF_4$@SiO_2 and NYEM@$NaScF_4$@SiO_2@Cu_2S dispersed in PBS solution *versus* (a) excitation time and (b) power density. (c) Digital photos of *E. coli* incubated within various conditions.

increment of 18 K, which is effective enough to kill the tumor cells during the PTT process.[56] However, only a tiny temperature variation of approximately 4.9 K can be observed in NYEM@$NaScF_4$@SiO_2 due to the absence of the strong NIR absorption of the Cu_2S NPs. Meanwhile, the excitation density dependent photothermal effect of NYEM@$NaScF_4$@SiO_2 and NYEM@$NaScF_4$@SiO_2@Cu_2S are also explored with a fixed exposure time of three minutes, both of which show a linear relationship with the increasing power density, as depicted in Fig. 5(b). Obviously, the temperature increasing rate of NYEM@$NaScF_4$@SiO_2@Cu_2S is much faster than that of NYEM@$NaScF_4$@SiO_2, benefiting from the outstanding light-to-heat conversion capacity of the Cu_2S NPs. In addition, a 980 nm wavelength is used for the detection of the photothermal conversion effect of NYEM@$NaScF_4$@SiO_2@Cu_2S dispersed in PBS solution. As shown in Fig. 5(a) and (b), the excitation wavelength of 980 nm can induce a larger maximum temperature and a faster heating rate than 915 nm under the same testing conditions, caused by the significant 980 nm-photon absorption of water in the PBS solution, which should be avoided to protect normal tissues from overheating in practical applications. Moreover, as depicted in Fig. S3,† the temperature of the blank PBS solution increased more rapidly under the excitation of 980 nm wavelength than that of the 915 nm wavelength, which further demonstrates the strong 980 nm-photon absorption of water. The above results present the tremendous potential of 915 nm-driven NYEM@$NaScF_4$@SiO_2@Cu_2S for PTT.

Subsequently, NYEM@$NaScF_4$@SiO_2@Cu_2S is attempted to be utilized for ablating *E. coli* through its own light-to-heat conversion ability to further evaluate its photothermal performance. Four groups of bacterial colonies with almost the same amount of *E. coli* are incubated in PBS buffer solution with or without NYEM@$NaScF_4$@SiO_2@Cu_2S NPs, named Group control, Group NIR, Group UCNPs and Group UCNPs + NIR, respectively. Meanwhile, both Group NIR and Group UCNPs + NIR are irradiated by 915 nm light with a power density of 12 mW mm^{-2} for 15 min before the incubation process. Fig. 5(c) shows the digital photos of the four experimental groups, which are simultaneously incubated in the same constant temperature incubator at 37 °C for 24 h. Evidently, the amount of *E. coli* existing in Group NIR and Group UCNPs is similar to that in the Group control, indicating the uselessness of employing NIR light exposure or Cu_2S-modified NPs independently. In contrast, very few bacteria survived in Group UCNPs + NIR, demonstrating the remarkable performance of NYEM@$NaScF_4$@SiO_2@Cu_2S NPs for photothermal conversion under the excitation of 915 nm wavelength.

In addition, an *ex vivo* experiment is designed to further assess the photothermal conversion and real-time temperature sensing ability of the NYEM@$NaScF_4$@SiO_2@Cu_2S NPs in subcutaneous tissue. Firstly, 200 μL PBS solutions containing NYEM@$NaScF_4$@SiO_2@Cu_2S (1 mg mL^{-1}) are subcutaneously injected into chicken tissue under around 2 mm thickness and then the chicken tissue is irradiated by 915 nm laser with various power densities for 3 min. Meanwhile, the FIR-based optical thermometer is utilized to monitor the subcutaneous temperature and infrared thermography is employed to detect the surface temperature of the chicken tissue. Distinctly, as shown in Fig. 6, the irradiation of the 915 nm laser almost has no effect on the temperature of chicken tissue without NPs. However, the subcutaneous temperature and surface temperature of the chicken tissue injected with Cu_2S-modified NPs

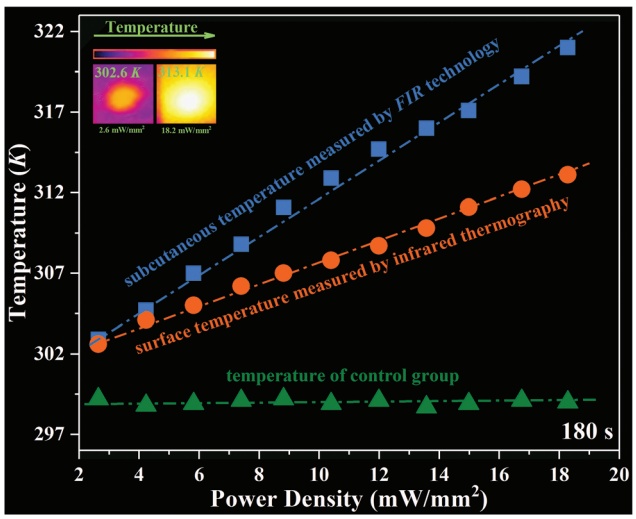

Fig. 6 The subcutaneous temperature and surface temperature of chicken tissue injected with NYEM@$NaScF_4$@SiO_2@Cu_2S NPs *versus* the power density of the 915 nm laser and chicken tissue without NPs is used as the control group.

both increased linearly with the increasing power density due to the remarkable photothermal conversion properties of Cu_2S NPs, which also exhibits the outstanding temperature sensing performance of NYEM@$NaScF_4$@SiO_2@Cu_2S NPs. The surface temperature is obviously lower than the subcutaneous temperature, which results from the heat diffusion in the tissue and heat loss from the surface of the tissue to the air.[20]

Conclusions

In summary, NYEM@$NaScF_4$@SiO_2@Cu_2S NPs with a central-satellite structure are successfully constructed through electrostatic interaction, which integrated the PTT function with real-time temperature monitoring. Instead of a 980 nm wavelength, 915 nm is employed as the excitation wavelength to pump the Yb^{3+} ions, by which the laser induced overheating effect for the biological tissues is effectively eliminated. Real-time temperature detection is realized by the FIR between the thermally coupled Stark sublevels of the Er^{3+}: $^4F_{9/2}$ manifold. The FIR-based optical thermometer shows a maximal S_A of 0.54% K^{-1} at 298 K and its S_R can be expressed as $490/T^2$. Importantly, its temperature resolution δT is better than 0.08 K over the biophysical temperature range with a minimal value of 0.06 K at 298 K, perfectly meeting the requirements of biomedicine. The photothermal conversion performance of NYEM@$NaScF_4$@SiO_2@Cu_2S is demonstrated to originate mainly from the ultra-small Cu_2S NPs by a simple contrast experiment. Moreover, the outstanding light-to-heat conversion ability of NYEM@$NaScF_4$@SiO_2@Cu_2S is further certified by photothermal ablation testing of *E. coli*, in which the overwhelming majority of bacteria are killed by the heat converted from the Cu_2S-modified NPs. All the results indicate that NYEM@$NaScF_4$@SiO_2@Cu_2S is a promising candidate for PTT along with high-resolution optical thermometry in real time.

Conflicts of interest

There are no conflicts to declare.

Acknowledgements

This work is financially supported by the National Natural Science Foundation of China (11704054, 11874055, 12004061, and 12004062) and the Science and Technology Research Program of Chongqing Municipal Education Commission (KJZD-K201800602 and KJZD-M202000601).

References

1 S. Liu, X. T. Pan and H. Y. Liu, *Angew. Chem.*, 2020, **132**, 5943–5953.
2 D. F. Zhi, T. Yang, J. O'Hagan, S. B. Zhang and R. F. Donnelly, *J. Controlled Release*, 2020, **325**, 52–71.
3 X. Li, F. J. Lovell, J. Y. Yoon and X. Y. Chen, *Nat. Rev. Clin. Oncol.*, 2020, **17**, 657–674.
4 T. Y. Shang, X. Y. Yu, S. S. Han and B. Yang, *Biomater. Sci.*, 2020, **8**, 5241–5259.
5 N. Fernandes, C. F. Rodrigues, A. F. Moreira and I. J. Correia, *Biomater. Sci.*, 2020, **8**, 2990–3020.
6 J. H. Chen, Y. C. Ma, W. Du, T. Y. Dai, Y. F. Wang, W. Jiang, Y. F. Wan, Y. C. Wang, G. L. Liang and G. F. Wang, *Adv. Funct. Mater.*, 2020, **30**, 2001566.
7 T. A. Tabish, P. Dey, S. Mosca, M. Salimi, F. Palombo, P. Matousek and N. Stone, *Adv. Sci.*, 2020, **7**, 1903441.
8 S. A. Zhao, R. R. Tian, B. Q. Shao, Y. Feng, S. W. Yuan, L. P. Dong, L. Zhang, K. Liu, Z. X. Wang and H. P. You, *ACS Appl. Mater. Interfaces*, 2019, **11**, 394–402.
9 J. Jiang, X. Che, Y. W. Qian, L. Z. Y. Wang, Y. Zhang and Z. L. Wang, *Front. Mater.*, 2020, **7**, 234.
10 Z. Zhou, B. W. Li, C. Shen, D. Wu, H. C. Fan, J. Q. Zhao, H. Li, Z. Y. Zeng, Z. M. Luo, L. F. Ma and C. L. Tan, *Small*, 2020, **16**, e2004173.
11 R. H. Yang, R. D. Li, L. Zhang, Z. G. Xu, Y. J. Kang and P. Xue, *J. Mater. Chem. B*, 2020, **8**, 7766–7776.
12 C. Y. Zhang, W. N. Wang, Z. Y. Chu and H. S. Qian, *Langmuir*, 2020, **36**, 1523–1529.
13 H. Y. Lu, Q. F. Zhao, X. D. Wang, Y. L. Mao, C. S. Chen, Y. K. Gao, C. S. Sun and S. L. Wang, *Colloids Surf., B*, 2020, **190**, 110941.
14 Y. T. Shen, X. Zhang, L. J. Liang, J. Yue, D. S. Huang, W. Q. Xu, W. Shi, C. Y. Liang and S. P. Xu, *Carbon*, 2020, **156**, 558–567.
15 Y. Yang, D. M. Zhu, Y. Liu, B. Jiang, W. Jiang, X. Y. Yan and K. L. Fan, *Nanoscale*, 2020, **12**, 13548–13557.
16 P. T. M. Phuong, H. J. Won, A. I. Robby, S. G. Kim, G. B. Im, S. H. Bhang, G. Lee and S. Y. Park, *ACS Appl. Mater. Interfaces*, 2020, **12**, 37929–37942.
17 M. Q. Sun, X. Q. Fu, K. X. Chen and H. Wang, *ACS Appl. Mater. Interfaces*, 2020, **12**, 46146–46161.
18 S. H. Zheng, Z. Jin, C. P. Han, J. J. Li, H. Xu, S. Park, J. O. Park, E. Choi and K. Xu, *J. Mater. Sci.*, 2019, **55**, 1184–1197.
19 C. G. Liu, H. X. Tang, X. Zheng, D. Y. Yang, Y. Zhang, J. T. Zhang, R. K. Kankala, S. B. Wang, G. Liu and A. Z. Chen, *ACS Appl. Mater. Interfaces*, 2020, **12**, 40673–40683.
20 H. Suo, X. Q. Zhao, Z. Y. Zhang, Y. F. Wu and C. F. Guo, *ACS Appl. Mater. Interfaces*, 2018, **10**, 39912–39920.
21 Z. H. Zou, J. Sun, Q. Li, Y. Pu, J. Q. Liu, R. Q. Sun, L. Y. Wang and T. G. Jiang, *Colloids Surf., B*, 2020, **189**, 110875.
22 T. C. Cetas and W. G. Connor, *Med. Phys.*, 1978, **5**, 79–91.
23 M. Lin, L. J. Xie, Z. J. Wang, B. S. Richards, G. J. Gao and J. P. Zhong, *J. Mater. Chem. C*, 2019, **7**, 2971–2977.
24 L. P. Li, F. Qin, Y. D. Zheng and Z. G. Zhang, *Opt. Mater. Express*, 2019, **9**, 3260–3267.
25 X. N. Chai, J. Li, X. S. Wang, Y. X. Li and X. Yao, *RSC Adv.*, 2017, **7**, 40046–40052.

26 H. Suo, F. F. Hu, X. Q. Zhao, Z. Y. Zhang, T. Li, C. K. Duan, M. Yin and C. F. Guo, *J. Mater. Chem. C*, 2017, **5**, 1501–1507.
27 Y. F. Shang, Q. Han, S. W. Hao, T. Chen, Y. Y. Zhu, Z. Y. Wang and C. H. Yang, *ACS Appl. Mater. Interfaces*, 2019, **11**, 42455–42461.
28 A. H. Zhou, F. Song, F. F. Song, M. Feng, K. Adnan, D. D. Ju and X. Q. Wang, *Opt. Mater.*, 2018, **78**, 438–444.
29 X. Liu, T. Li, X. Q. Zhao, H. Suo, Z. Y. Zhang, P. J. Zhao, S. Gao and M. Niu, *Dalton Trans.*, 2018, **47**, 6713–6721.
30 G. C. Jiang, S. S. Zhou, X. T. Wei, Y. H. Chen, C. K. Duan, M. Yin, B. Yang and W. W. Cao, *RSC Adv.*, 2016, **6**, 11795–11801.
31 E. C. Ximendes, U. Rocha, C. Jacinto, K. U. Kumar, D. Bravo, F. J. Lopez, E. M. Rodriguez, J. Garcia-Sole and D. Jaque, *Nanoscale*, 2016, **8**, 3057–3066.
32 X. F. Wang, Q. Liu, Y. Y. Bu, C. S. Liu, T. Liu and X. H. Yan, *RSC Adv.*, 2015, **5**, 86219–86236.
33 E. M. Dianov, *Light Sci. Appl.*, 2012, **1**, e12.
34 J. H. Zhang, Z. D. Hao, J. Li, X. Zhang, Y. S. Luo and G. H. Pan, *Light Sci. Appl.*, 2015, **4**, e239.
35 K. C. Liu, Z. Y. Zhang, C. X. Shan, Z. Q. Feng, J. S. Li, C. L. Song, Y. N. Bao, X. H. Qi and B. Dong, *Light Sci. Appl.*, 2016, **5**, e16136.
36 F. Wang, S. H. Wen, H. He, B. M. Wang, Z. G. Zhou, O. Shimoni and D. Y. Jin, *Light Sci. Appl.*, 2018, **7**, 18007.
37 H. Zhang, J. T. Ye, X. L. Wang, S. L. Zhao, R. S. Lei, L. H. Huang and S. Q. Xu, *J. Mater. Chem. C*, 2019, **7**, 15269–15275.
38 G. F. Liu, Z. Sun, Z. L. Fu, L. Ma and X. J. Wang, *Talanta*, 2017, **169**, 181–188.
39 M. Back, E. Casagrande, C. A. Brondin, E. Ambrosi, D. Cristofori, J. Ueda, S. Tanabe, E. Trave and P. Riello, *ACS Appl. Nano Mater.*, 2020, **3**, 2594–2604.
40 Z. Y. Zhao, K. Li, C. Liu, Q. Y. Yin, J. J. Han and J. Heo, *J. Mater. Chem. C*, 2019, **7**, 6134–6143.
41 Z. Y. Zhang, H. Suo, X. Q. Zhao and C. F. Guo, *Photonics Res.*, 2020, **8**, 32–38.
42 H. Suo, X. Q. Zhao, Z. Y. Zhang, T. Li, E. M. Goldys and C. F. Guo, *Chem. Eng. J.*, 2017, **313**, 65–73.
43 H. Suo, C. F. Guo and T. Li, *J. Phys. Chem. C*, 2016, **120**, 2914–2924.
44 Y. N. Huang, Q. B. Xiao, H. S. Hu, K. C. Zhang, Y. M. Feng, F. J. Li, J. Wang, X. G. Ding, J. Jiang, Y. F. Li, L. Y. Shi and H. Z. Lin, *Small*, 2016, **12**, 4200–4210.
45 Q. Q. Zhan, J. Qian, H. J. Liang, G. Somesfalean, D. Wang, S. L. He, Z. G. Zhang and S. Andersson-Engels, *ACS Nano*, 2011, **5**, 3744–3757.
46 G. T. Xiang, X. T. Liu, J. H. Zhang, Z. Liu, W. Liu, Y. Ma, S. Jiang, X. Tang, X. J. Zhou, L. Li and Y. Jin, *Inorg. Chem.*, 2019, **58**, 8245–8252.
47 G. T. Xiang, X. T. Liu, W. Liu, B. Wang, Z. Liu, S. Jiang, X. Zhou, L. Li, Y. Jin and J. H. Zhang, *J. Am. Ceram. Soc.*, 2019, **103**, 2540–2547.
48 G. T. Xiang, X. T. Liu, Q. Xia, S. Jiang, X. J. Zhou, L. Li, Y. Jin, L. Ma, X. J. Wang and J. H. Zhang, *Inorg. Chem.*, 2020, **59**, 11054–11060.
49 G. T. Xiang, Q. Xia, X. T. Liu and X. J. Wang, *Dalton Trans.*, 2020, **49**, 17115–17120.
50 G. T. Xiang, X. T. Liu, Q. Xia, X. C. Liu, S. Xu, S. Jiang, X. J. Zhou, L. Li, D. Wu, L. Ma, X. J. Wang and J. H. Zhang, *Talanta*, 2021, **224**, 121832.
51 I. E. Kolesnikov, A. A. Kalinichev, M. A. Kurochkin, D. V. Mamonova, E. Y. Kolesnikov, E. Lahderanta and M. D. Mikhailov, *Nanotechnology*, 2019, **30**, 145501.
52 Z. Y. Zhang, H. Suo, X. Q. Zhao, D. Sun, L. Fan and C. F. Guo, *ACS Appl. Mater. Interfaces*, 2018, **10**, 14570–14576.
53 R. C. Lv, P. P. Yang, F. He, S. L. Gai, G. X. Yang and J. Lin, *Chem. Mater.*, 2015, **27**, 483–496.
54 G. T. Xiang, J. H. Zhang, Z. D. Hao, X. Zhang, G. H. Pan, Y. S. Luo, W. Lu and H. F. Zhao, *Inorg. Chem.*, 2015, **54**, 3921–3928.
55 X. Zhou, Y. J. Wang, H. W. Wang, L. Xiang, Y. L. Yan, L. Li, G. T. Xiang, Y. H. Li, S. Jiang, X. Tang and X. J. Zhou, *Sens. Biosensing Res.*, 2020, **29**, 100345.
56 E. C. Ximendes, U. Rocha, C. Jacinto, K. U. Kumar, D. Bravo, F. J. Lopez, E. M. Rodriguez, J. Garcia-Sole and D. Jaque, *Nanoscale*, 2016, **8**, 3057–3066.